Article

Multifunctional integrated pattern for enhancing fog harvesting water unidirectional transport in a heterogeneous pattern

Check for updates

Daejeong Yang ⓘ, A. G. Ramu ⓘ & Dongjin Choi ⓘ ✉

Solid surfaces with improved wettability as well as geometric structures can enhance capture and droplet removal, thereby improving fog harvesting. We fabricated Al wires by combining superhydrophilic (SHL), superhydrophobic (SHB), and oil-infused SHB (SHBO) surfaces into a pattern whose fog-harvesting efficiency could be measured. The SHL-SHBO-SHL pattern showed the highest promise of water droplet capture and mobility on a solid surface with 42% efficiency compared to the 34% efficiency of Bare. In order to identify the optimal efficiency features, two boundary conditions (boundary I: from SHL to SHBO and boundary II: from SHBO to SHL) were introduced, and the impact of the hydrophilic area was examined. Boundary I boosts capture efficiency whereas boundary II increases drain efficiency. Understanding the forces operating at the wettability gradient surface, as well as incorporating the area ratio of SHL and SHBO via wettability combinations, are key to designing effective fog harvesting systems.

The insufficient supply of fresh water poses a significant risk to the continued existence of all living things, including humans. Abnormal climate phenomena, such as heat waves, floods, heavy snowfalls, and droughts, due to global warming are increasing rapidly[1,2], thus unbalancing the ecosystem and exacerbating the shortage of fresh water[3]. To overcome this issue, researchers have been exploring techniques for harvesting water from creatures (animals and plants, such as the Namib Desert beetle[4,5], thorny devil dragon[6,7], bushman grass[8,9], and cactus[10,11]) based on how these creatures harvest atmospheric water. However, effective water harvesting from the surrounding air remains a serious challenge[12]. Among atmospheric moistures, fog harvesting is the most fascinating, as it does not require additional energy even though it is accompanied by regional limitations. As there are no phase changes, as well as thermal exchange, in the fog-harvesting process, their mechanisms can be simplified into the capture, coalescence, growth, and removal of surface water droplets.

The biomimetic perspective[13] reveals that fog harvesting can be divided into two categories. The first one involves developing a topological design and overall geometric structure for the fog harvester. For example, the conical, furrow, and slender shape of a cactus, beetle, and bushman plant are references, respectively; the structures of these creatures comprise micro- or nanostructures. The second category involves the optimal combination of wettability features to enhance the water-collecting efficiency. The previous researcher attempted single bio inspired designs, which could not yield an efficient fog harvester; however, recent studies combined two or more bio-inspired designs. Wong et al. proposed hydrophilic directional slippery rough surfaces, which combined rice leaves and pitcher plants as excellent surfaces for air-water collectors[14]. Zhigang et al. designed a multi-bio-inspired fog system by combining a venation-like pattern with a beetle-like hybrid-wettability pattern[15]. According to recent reports, surface wettability can easily boost the enjoyment of moisture harvesting; nevertheless, depending on the circumstances, various results have been noted. It's also unclear what kind of surface wettability would be ideal for effective water collecting[16].

In this study, a multi-bio-inspired fog-harvesting system was developed by combining a bushman-grass-like wire structure with the Namib-Desert-beetle-like wettability pattern (Fig. 1a). The function of bumps on the backs of many other insects was found to be unclear by J. Guadarrama-Cetina et al.[17]. These beetles' backs might gather both fog and dew at locations where the distinction between the two occurrences was not made. However, the biomimetic beetle shell employed in this work concentrated
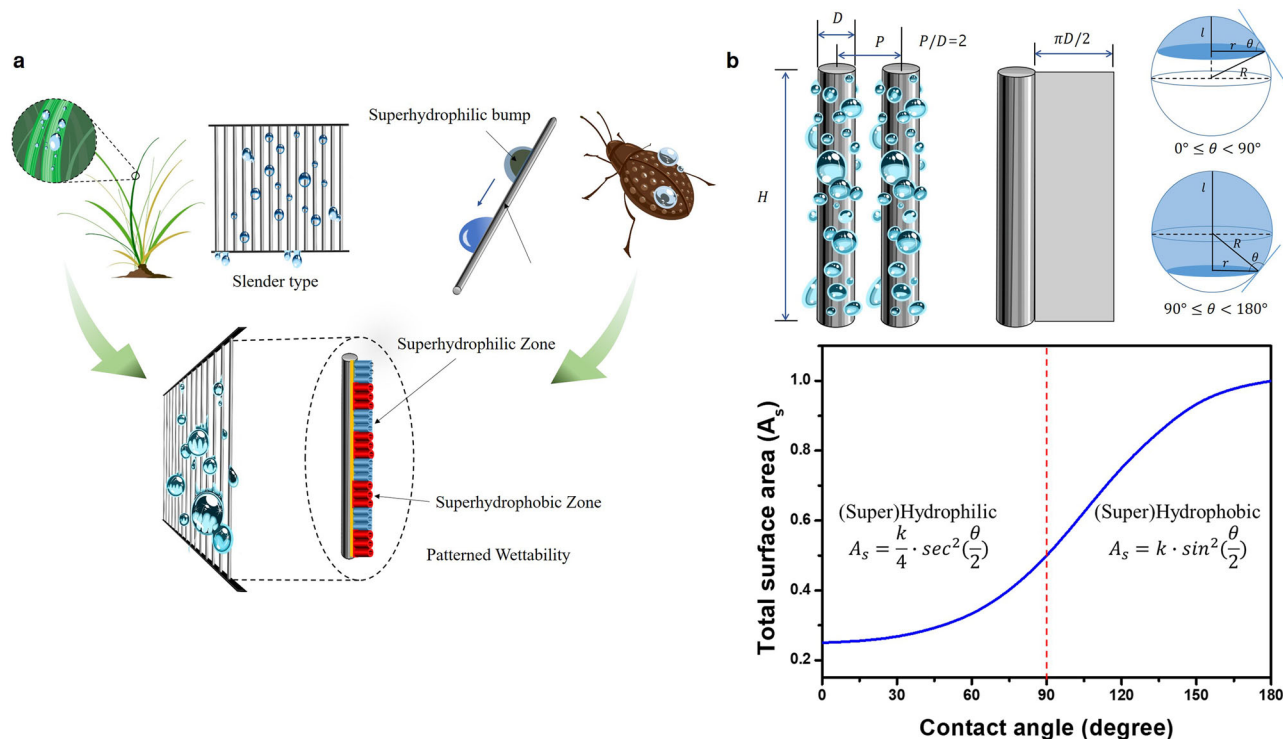
School of Materials Science and Engineering, Hongik University 2639, Sejong-ro, Jochiwon-eup Sejong city, Sejong 30016, South Korea.
✉e-mail: djchoi@hongik.ac.kr

Fig. 1 | Hydrophilic and Hydrophobic directional boundaries inspired by bushman grass and Namib beetle-like pattern. a Overview of the combination between structures like bushman grass and patterned wettability like the back surface of Namib beetle. **b** Surface area of cap-shaped droplets of wire covered with SHL and SHB.

on capturing and moving mist droplets to blend wet properties. Numerous studies have demonstrated how the design with wire structures rather than plates improves water collection[9,18,19]. However, only a few studies have been considered the wettability patterning of each wire to further enhance the efficiency of this wire-type fog-harvesting device. The SHB surface showed a larger surface area than the SHL surface following the Supplementary Equations 1–2 for cap-shaped water droplets (Fig. 1b) in the state that the surface roughness was ignored. Numerous experimental studies have demonstrated that hydrophobic surfaces exhibit higher water-collection capacities than hydrophilic surfaces. Jin et al. compared the fog-harvesting capacities of the SHB and SHL plate surfaces, as well as patterned surfaces, reporting that the SHB surfaces exhibited superior capacities compared with the SHL surfaces[20]. Additionally, employing heterogeneous structures can enhance fog harvesting by improving capture efficiency and enabling directional transport through mechanisms such as top-induced flipping[21]. Therefore, we revealed the effect of the wire structure in which the wettability is patterned on the water-droplet capture and mobility. Furthermore, the surface properties of solids for efficient fog collection were observed with the proper harmony of the superhydrophilicity (SHL) and superhydrophobicity (SHB) of the nanostructured rough wire surfaces.

Results
Water-collection rate and efficiency
The SHB oil-infused (SHBO) frame can be developed, following Fig. 2a. The detailed synthesis method was covered in the method section.

We designed a fog collection device as shown in Supplementary Fig. 1 by adopting the turbulent jet theory of Cushman-Roisin to collect the maximum amount of fog that could be obtained[22]. Schemenauer and Joe indicated an optimum wind speed of 3.5 m/s for optimal efficiency, as higher wind speeds are inversely proportional to the liquid water content and reflect higher values of water collecting efficiency[23]. The yields from collecting water are influenced by numerous factors, wind velocity is the most crucial component; other elements include mesh properties, droplet size distribution, and fog liquid water content[24]. Supplementary Fig. 2a and Supplementary Movies 1-4 displays the optical views of real-time

observations of the fog-harvesting operations of the BARE, SHB (A-2_CVD-S, A-4_CVD-S), and SHBO (A-2_CVD-S_CVD-K, A-4_CVD-S_CVD-K) frames. Generally, the fog droplets on the SHBO surface were captured, grown, combined rapidly, and moved rapidly to the water repository. Patterning, as illustrated in Supplementary Fig. 2b is a combination of SHL and SHBO and was created at a constant ratio because SHBO has the best fog-harvesting performance. Figure 2b shows the water deposition on the surface based on the three-dimensional (3D) structure and wetting characteristics in 5 min. The flooding at the end of the sample, which is represented by the difference in water collecting efficiency, is the largest difference between the nano-structure of 2 and 4 min. The dropwise collections on the SHB and SHBO surfaces, as well as the filmwise collection on the SHL surface, are evidently displayed in the patterned SHL-SHBO. Therefore, even if the pattern was the same, the 4 min-anodized samples, i.e., the without-flooding sample, exhibited the highest fog-harvesting efficiency (Fig. 2c). Figure 2d shows the water-collection ratio as collecting water (W_c) per unit time (min) and unit area (cm^2) in 30 min. The water-collection rates of the patterned SHL-SHBO samples with 2 and 4 min increased by 117.7% and 124.8% and their efficiencies were enhanced by 110.8% and 120.9%, respectively, compared with those of the non-patterned samples. The water-collection rates and efficiencies of all the samples (Supplementary Table 1) are shown in Supplementary Fig. 3. Regardless of the thickness of the nanostructure, the most efficient pattern was the SHL–SHBO–SHL arrangement. The patterning of wettability improved the water-collection rate and efficiency of the fog harvester and affected the ratios and alignment orders of the patterns in Supplementary Fig. 4 and Fig. 2c, e.

Further, β is defined as the area ratio of SHL (A_{philic}) to SHBO (A_{phobic}).

$$\beta = \frac{A_{philic}}{A_{phobic}} \qquad (1)$$

Figure 2e and Supplementary Table 1 presents β, which is the area ratio of the wetting characteristics of each sample, and the fog-harvesting efficiency (η_w), accordingly. We observed that the larger the finite number β (=2) and the more the total number n (=4) of boundaries (Boundaries I and
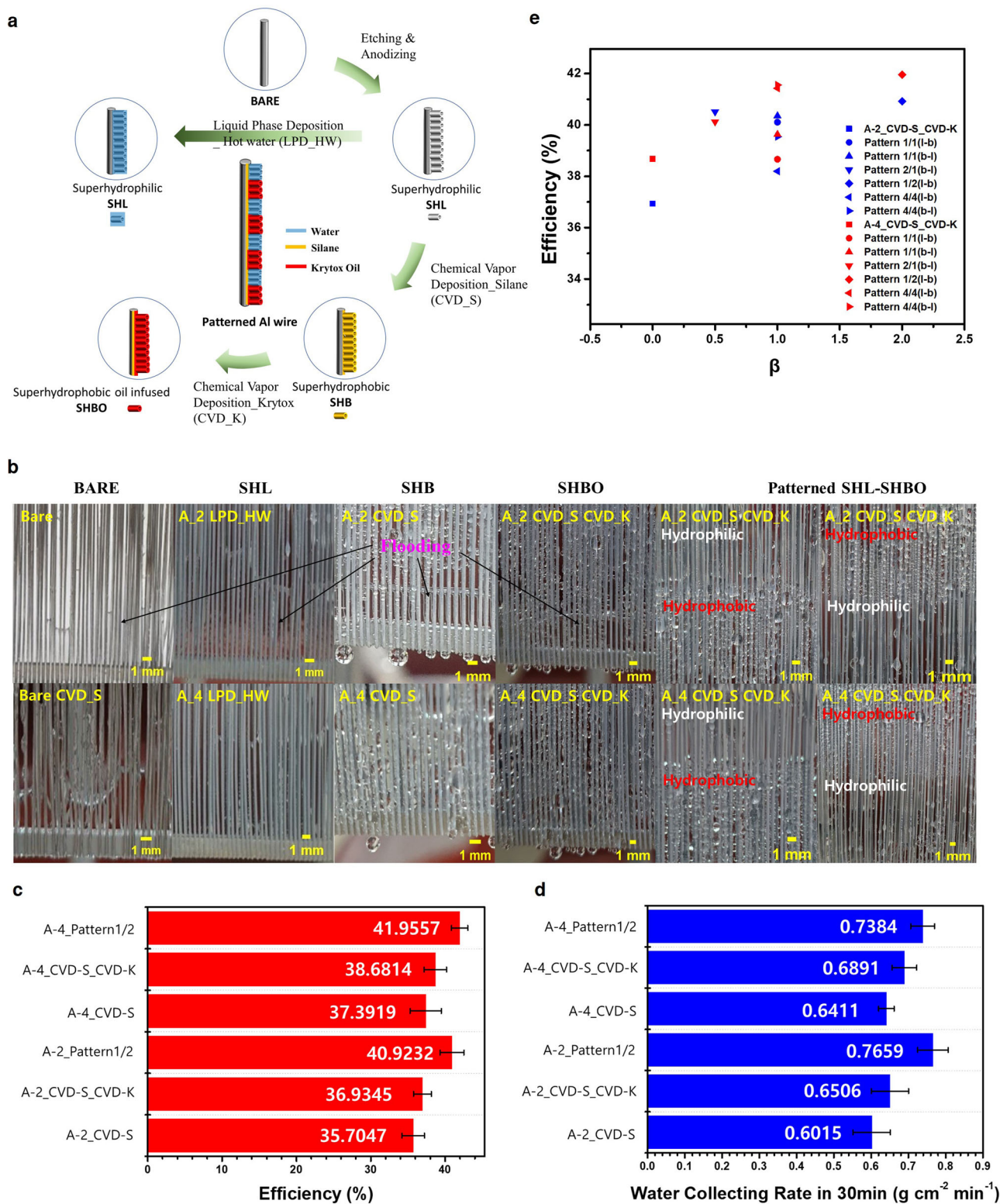
Fig. 2 | Materials with 3D frameworks. a Schematic showing of the fabrication process of BARE, SHL, SHB, and SHBO. **b** Optical harvesting images of various experiment conditions in 5 min. **c, d** Water collection rate (g·cm⁻²·min⁻¹) and water collection efficiency for 30 min of each sample. A-2-pattern 1/2 surface has a large number of nucleation sites, resulting in efficient water collecting performances. **e** Fog collection efficiency as a function of β on the patterned surface of SHBO and SBL. The standard deviation from five separate experiments is shown by error bars.

II), the higher the fog-harvesting efficiency (A-4_pattern1/2, $\eta_w = 41.9557$). Even in the same β, except for A-2_pattern1/1, the case in which A_{phobic} is at the top exhibited better fog efficiency characteristics. It means that Boundary II acts more influential than Boundary I. The surface energy gradient is influenced by surface roughness and chemical composition, and it facilitates the liquid's movement towards the wetter zone[25,26]. Furthermore, We have analyzed the mass percentage of krytox oil in the collected water Supplementary Fig. 8 depicts the mass percentage of oil present in the

water that was collected. A larger starting quantity of oil results in an increased proportion of oil in the water, reaching a maximum of roughly 0.08% for SHL-SHBO-SHL -5 μm after 6 days of fog harvesting[27]. The contact angle data validate the existence of a consistently thin layer of oil during the 70-day operation. Furthermore, the substantial contact angle of SHL-SHBO-SHL further substantiated the durability of the oil coating, so establishing the SHL-SHBO-SHL pattern as exhibiting exceptional fog harvesting capabilities.

Structural designs for an efficient fog harvester
To enhance the fog-harvesting efficiency, the surface area of the sample to be contacted by the fog droplets must be widened to capture the droplets hitting the surface and move them to the reservoir most rapidly and frequently with the smallest volume. Effective surface area expansion can be expected in the structural design of fog harvesters. Numerous studies have demonstrated the efficiency of fog-harvesting devices in various structures, including the geometrical design, size, and slope. For example, Noman et al. reported that different types of mesh structures, such as common raschel, rhombus, and woven mesh structures, act as major determining factors of fog-harvesting efficiency and explored how ultraviolet (UV) radiation, corrosion resistance, and robustness to strong winds can be blocked[24]. Boreyko et al. reported that harps fabricated with metal wire arrays could harvest fog three times more than meshes[18].

The micro- and nanostructured surfaces of many living things enable unique water-intake capabilities. Based on the features of a cactus, Jiang et al. implemented multiple structures and functions in the fog-harvesting system comprising conical spines and trichomes[28]. Based on the anodized micro/nanostructure of the 0.3 mm Al wire in Supplementary Fig. 5, the micro/nanostructures on the front and side of Fig. 3a were implemented. The 3D nanostructured Al surface, which was obtained by anodizing, can be divided into the front, side, and back depending on the face of directionally moving water droplets, the backside was not considered as it does not face the water droplets. Figure 3b shows that the front and side nanostructures were different; the front comprised nanotube channels with average pores of <50 nm and the side comprised a micro/nanostructure that is similar to a coral reef. Andrews et al. revealed the 3D hierarchical structures of a plant, Cotula fallax, and demonstrated how the compact structures greatly facilitated fog harvesting, where the 3D structures enhanced the surface-to-volume ratio and subsequently increased the water-capture efficiency[29]. The top and cross-section morphologies of the frontside exhibited nanochannel, interchannel, and side-hole distances of 20–90 nm, 120–200 nm, and 60–90 nm, respectively, in the A-2_CVD-S_CVD-K frame. Figure 3c shows the energy-dispersive X-ray spectroscopy (EDS) images of silane (Si, F) and the Krytox oil (C), which were uniformly deposited in the nanostructure via CVD.

Next, X-ray diffraction analysis was performed to further elucidate the bulk structure of the material. Supplementary Fig. 6 reveals that the internal structure of the primary structure differed slightly before and after the chemical treatment. The crystal lattice of the metal matrix, which was anticipated from the surface, was unaffected by the chemical treatment. Bare Al exhibits an osbornite phase with a strong (111) peak at 38.47°, a relatively weak (200) peak at 44.72°, and a weak (311) peak at 78.23°, whereas the chemically treated samples exhibited the strongest (200) peak, and the (111) peak exhibited very small peaks.

Surface roughness
In addition to the chemical composition, surface roughness represents a significant determining factor of surface wettability. Thus, inducing sufficient surface roughness in natural materials is a conventional procedure for generating SHB and SHL materials in Supplementary Fig. 7[29,30]. To generate SHB materials, two general guidelines can be summarized, as follows: induce sufficient roughness on the material surface and modify the chemical composition of the material surfaces to make them SHB, with a WCA of >90° [31,32].

The connection between wettability and roughness must be investigated as this outcome can be related to the numerous varieties of rough structures. The micro- and nano-scale roughness were measured by atomic

force microscopy (AFM) to assess the 3D topography of the as-prepared samples (Fig. 4 and Supplementary Table 2), indicating that the nano-scale roughness characteristics were readily apparent. The generally utilized roughness parameters include Ra, Rq, Rz, and Rsk, which correspond to the arithmetical mean deviation, root-mean-square average deviation, total height of ten points, and skewness, respectively, of the roughness profile. The nano-scale roughness of the samples was assessed using the 20×20 m^2 AFM 3D topographic pictures. Figure 4a–g shows that a longer anodizing time corresponded to relatively low roughness, although this was because of the inclusion of many nanostructures. Within the same anodizing time group, chemical coating and WCA correlated with the roughness. Namely, as the chemical treatment proceeded, Ra increased, and the hydrophobicity became considerably greater than the hydrophilicity. Based on the WCAs of the samples (Fig. 4h), we inferred that a high nano-scale roughness was a prerequisite for imparting SHB. The plots of WCA against the surface-roughness parameters, Ra, Rq, Rz, and Rsk, are shown in Fig. 4i, j and Supplementary Table 2 to clarify the reliance of WCA on the micro- and nano-scale roughnesses. The Ra, Rq, and Rz plots against WCA did not demonstrate the dependence among the variables. However, Fig. 4j reveals that Rsk, which represents the symmetry of the surface height with respect to the mean plane, correlated with WCA. The SHB surface obtained by silane coating is Group A, with an Rsk value of 0.02–0.08, and the sample with Krytox oil represents the SHBO surface corresponding to Group B, with an Rsk value of 0.54–0.79. It is logical to assume that a surface comprising only nanostructures or microstructures would exhibit an extremely low Rsk value. Our findings regarding the relationship between the roughness characteristics and WCA corresponded well with those of the extant studies[33]. Those authors indicated that Rsk = 0 was preferable for achieving SHB surfaces. Another study revealed that the best SHB cornflower structure exhibited a high Rsk value (0.7–1.3), which resulted in improved SHB for hierarchical micro/nanostructures with sufficient height and aspect ratio based on lotus leaves (Rsk = ~1.075)[34]. Generally, hierarchical micro/nanostructures obtained significantly high Rsk values, and side of SHBO in this study were very similar to the hierarchical structure and exhibited optimal wettability to increase performance efficiency.

Surface-wetting design for an efficient water harvester
Surface wettability determines the collection mode of the droplet, and the water-collection rate varies with the collection mode. Wang et al. investigated three collection modes (no-, dropwise-, and filmwise-collection modes) as a function of the fluid–solid binding-force parameters using molecular dynamics simulation[35]. Therefore, to increase water collection, the surface wettability that can adequately facilitate the capture and flow of already condensed fog droplets in the air into the storage must be determined. Park et al. showed that by modifying the wet characteristics of the surface, cutting the wire radius, and optimizing the wire spacing, the fog collection efficiency of typical polyolefin meshes increased by five times[36]. Various experimental conditions were implemented to obtain the optimal surface wettability comprising hydrophilic and hydrophobic combinations. Figure 5a shows some samples with wetting properties under various conditions for fog harvesting. Water droplets on a rough surface (micro- and nanostructured) are present in the Wenzel and Cassie–Baxter states or in a mixture of both states. The biggest difference between both states is the presence or absence of air between the surface and droplets. The Wenzel and Cassie–Baxter states of the micro-sized wires are displayed as CA measurement images, and the collection state of the droplets is predicted by WCA. The A-2_CVD-S (163°) and A-4_CVD-S (169°) samples followed the Cassie–Baxter state under dry conditions and followed the Metastable and Cassie–Baxter states, under wet conditions, respectively. The oil-infused samples changed from the Metastable to Wenzel states based on the change from dry to wet conditions.

Although the Wenzel and Cassie–Baxter states may account for the geometric (roughness and fraction rates) and chemical (CA) heterogeneity effects, it is considerably challenging to forecast the states that a droplet would adopt on a given rough surface. To do this, it is necessary to examine
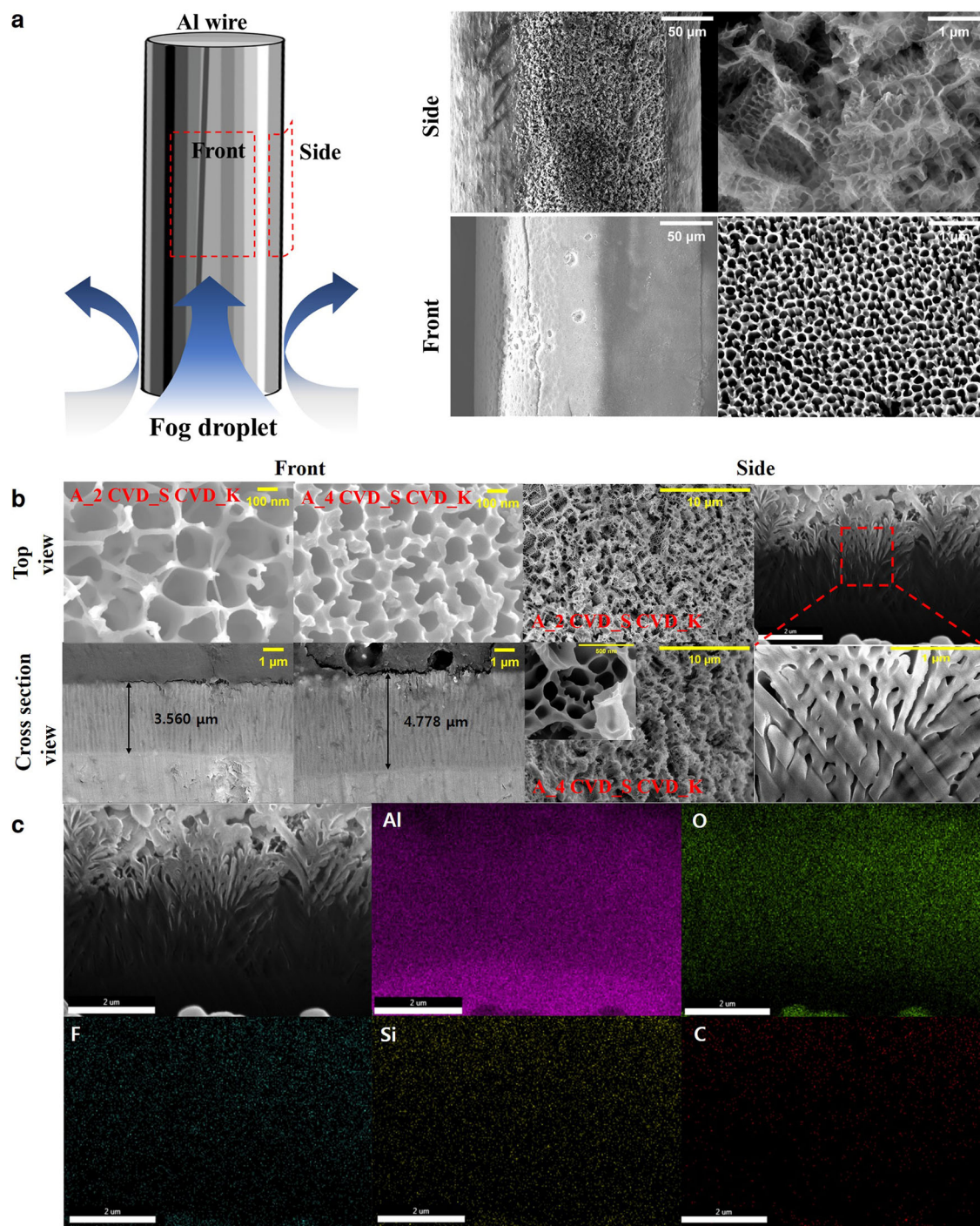
Fig. 3 | Surface morphology features of prepared pattern nanostructures. a Morphology of front and side of anodized Al wires. **b** SEM and FIB images of top and cross-sections for front and side region of A-2_CVD-S_CVD-K and A-4_CVD-S_CVD-K. **c** EDS of a cross-section of A-2_CVD-S_CVD-K.

the stabilities of both wetting states, particularly the Cassie–Baxter state. The Cassie–Baxter state, also known as the SHB state, may become unstable and change into the Wenzel state under specific conditions, such as vibration and pressure[37,38]. Additionally, this instability is more probable if the intrinsic solid surface exhibits a high air-trapped area percentage or is more hydrophilic[39]. There are numerous other elements, such as the spacing and sizes of surface structure units, geometric arrangements, and structure, that may impact wetting stability. For example, local convex-curvature structures can enhance the Cassie–Baxter stability[40]. Figure 5b–e show the results of a durability test for the sample surface for 78 days against corrosion and UV radiation factors, which exert the most influence when placing samples

in natural conditions. Surface WCA was measured while the sample was immersed in a 3.5% NaCl solution (Fig. 5b, c) and exposed to UV (Fig. 5d, e). Figure 5c, e show the measured surface WCA at 3 min intervals in a sample exhibiting hydrophilic properties to observe the change in F_{cap}, respectively. The 4 min-anodized samples were maintained the most stable properties over time. Namely, the surface characteristics of the micro/nanostructure were key to the durability of the surface.

Forces acting on water droplets

A motionless droplet on a solid surface is typically susceptible to external counterbalanced forces. However, this droplet will move in a certain
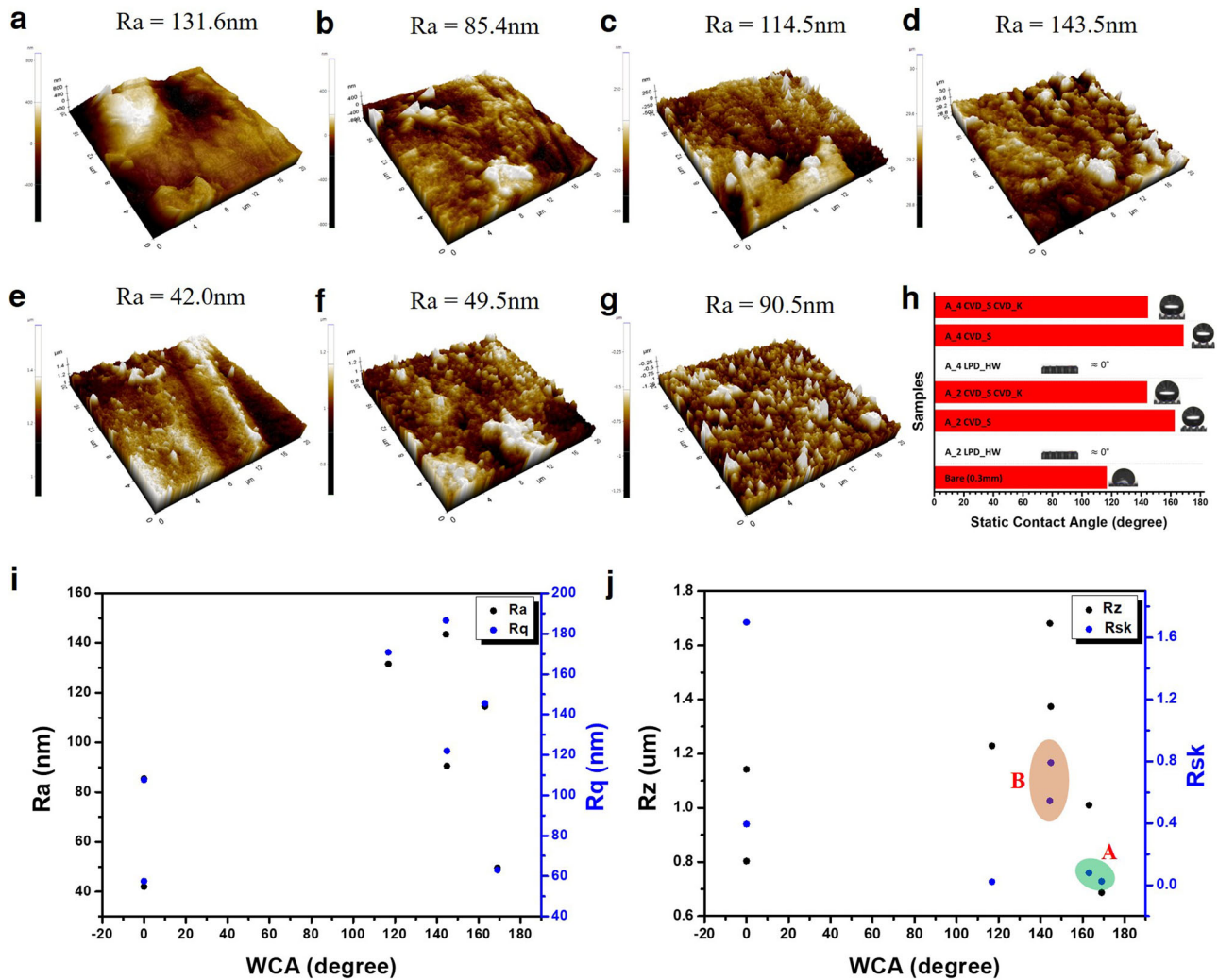
Fig. 4 | Atomic force microscopy 3D topographic image of the samples. a Bare. **b** A-2_LPD-HW. **c** A-2_CVD-S. **d** A-2_CVD-S_CVD-K. **e** A-4_LPD-HW. **f** A-4_CVD-S. **g** A-4_CVD-S_CVD-K. **h** Static contact angle of samples. **i** Ra and Rq vs the surface WCA. **j** Rz and Rsk vs the surface WCA.

direction if the external forces stop counterbalancing. These varied mobilities can be broadly divided into the following two categories: mobilities induced by asymmetrical geometric design of the substrate and mobilities induced by the nonuniform surface wettability[30].

Equation (2) is derived from the analysis of the force balance for a droplet moving over a heterogeneous surface. The driving force (F_{dri}) is derived from the variable surface energy (or wettable property) of the liquid–solid interface, whereas the resistance force (F_{res}) against F_{dri} is derived from the hysteresis force (F_{hys}) and viscous force (F_{vis}) before and during the flow of the droplet.

$$\sum F = F_{dri} - F_{res} = F_{dri} - F_{vis} - F_{hys} \qquad (2)$$

F_{dri} of a water droplet on a wettability gradient surface can be expressed using Eq. 3[39]

$$F_{dri} \cong \pi\gamma_w R_c^2 \left(\frac{dcos\theta_d}{dx}\right) \qquad (3)$$

where γ_w is surface tension of the water droplet, R_c is its contact radius on the solid, and θ_d is its dynamic contact angle (CA) with solid surfaces. Further, Eq. 3 shows that F_{dri} is proportional to the liquid–solid contact area (R_c^2) and

CA gradient od surface energy ($\frac{dcos\theta_d}{dx}$). The CA F_{hys} is written as Eq. 4[40]

$$F_{hys} = 2\gamma_w R_c \left(\cos\theta_{cr} - \cos\theta_{ca}\right) \qquad (4)$$

To initiate motion, it is necessary for a droplet to overcome a moving barrier. In Eq. 4 θ_{ca} and θ_{cr} represent the advancing and receding water CAs of the central droplet, respectively. The viscous force produced within the liquid during the motion of the gradient surface can be expressed as Eq. 5[41]:

$$F_{vis} \cong 3\pi\eta R_c u \ln\left(\frac{X_{max}}{X_{min}}\right) \qquad (5)$$

Where u and η denote the velocities of the moving droplet and liquid's viscosity, respectively. The characteristic lengths of the liquids, X_{min} and X_{max}, can be defined as the molecule length and droplet radius, respectively. The impact of the CA hysteresis (CAH) is not considered in the aforementioned treatment. In practice, the droplet cannot move until the force from the free-energy gradient exceeds a hysteresis-induced threshold force[39]. When the droplet travels steadily, F_{dri} is assumed to be equal ($F_{dri} = F_{vis}$), and u is computed in Eq. 6 as follows[41]:

$$u \cong \gamma_w R_c \left(\frac{dcos\theta_d}{dx}\right) / \left(3\eta\ln\left(\frac{X_{max}}{X_{min}}\right)\right) \qquad (6)$$
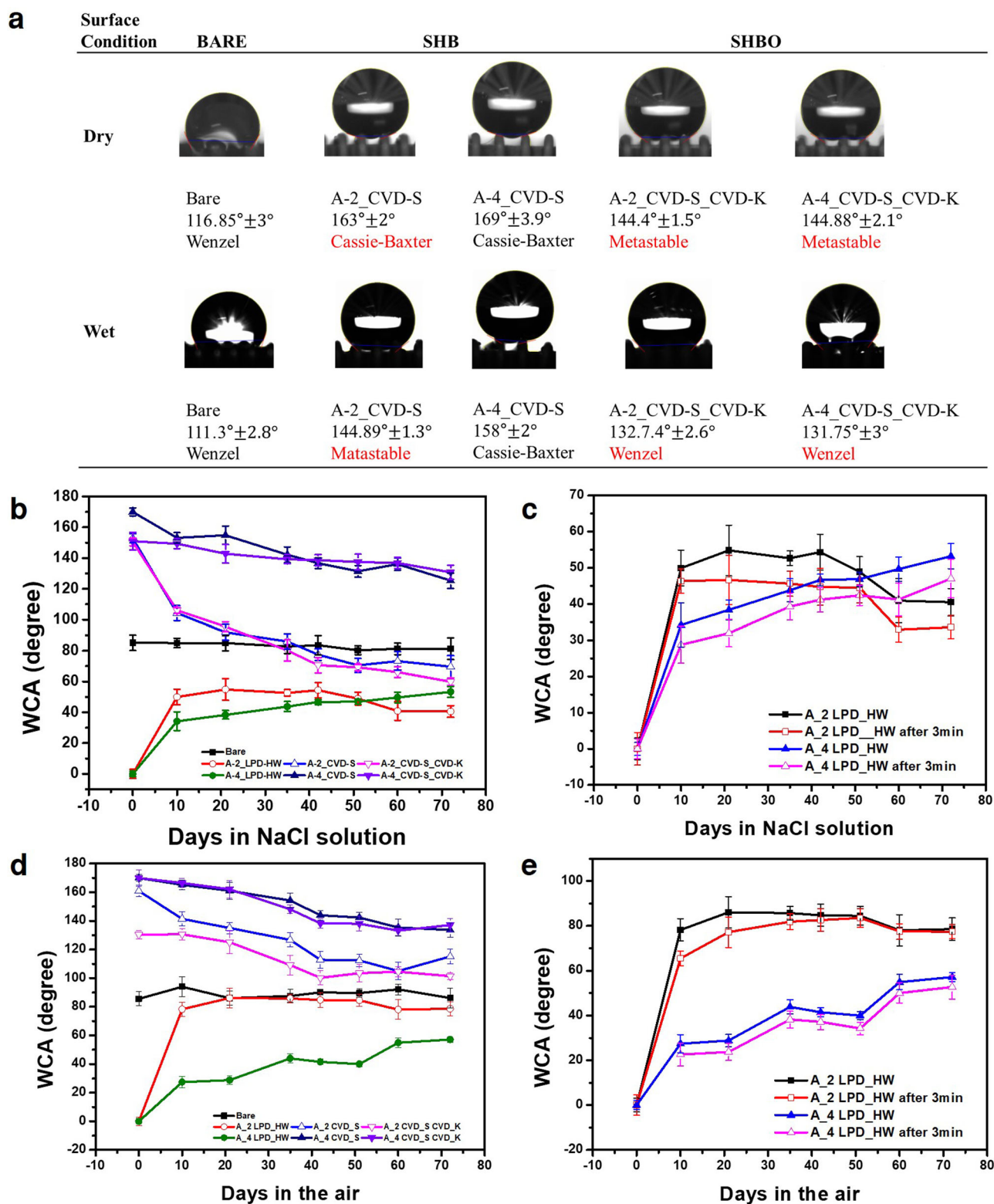
Fig. 5 | Wetting features of water droplets on prepared patterned nanostructures. **a** WCA and wettability states of each wire as a function of surface conditions (dry and wet). Surface WCA durability test of Al plates with same conditions for 78 days. **b**, **c** in the 3.5% NaCl solution. **d**, **e** under UV exposure in air. Error bars show the standard deviation five independent experiments.

Equation (6) reveals that u is inversely related to η, although it is proportional to γ_w, R_c, and $\frac{d\cos\theta_d}{dx}$.

Force analysis was performed to explore the basic mechanisms of the movement of droplets based on the four wettability states of the surface (Fig. 6a). Generally, the spherical-cap shape of the droplet

depended on the size and wettability characteristics of the surface. The larger the droplet, the greater the influence of gravity than the length of the capillary, $\beta^{-1} = \sqrt{\gamma_{LV}/\rho g}$, and the greater the F_{gra}, causing the droplet to flatten or fall[40]. The spherical surface of the droplet is a result of the surface tension governing gravity, which prefers to impose on a
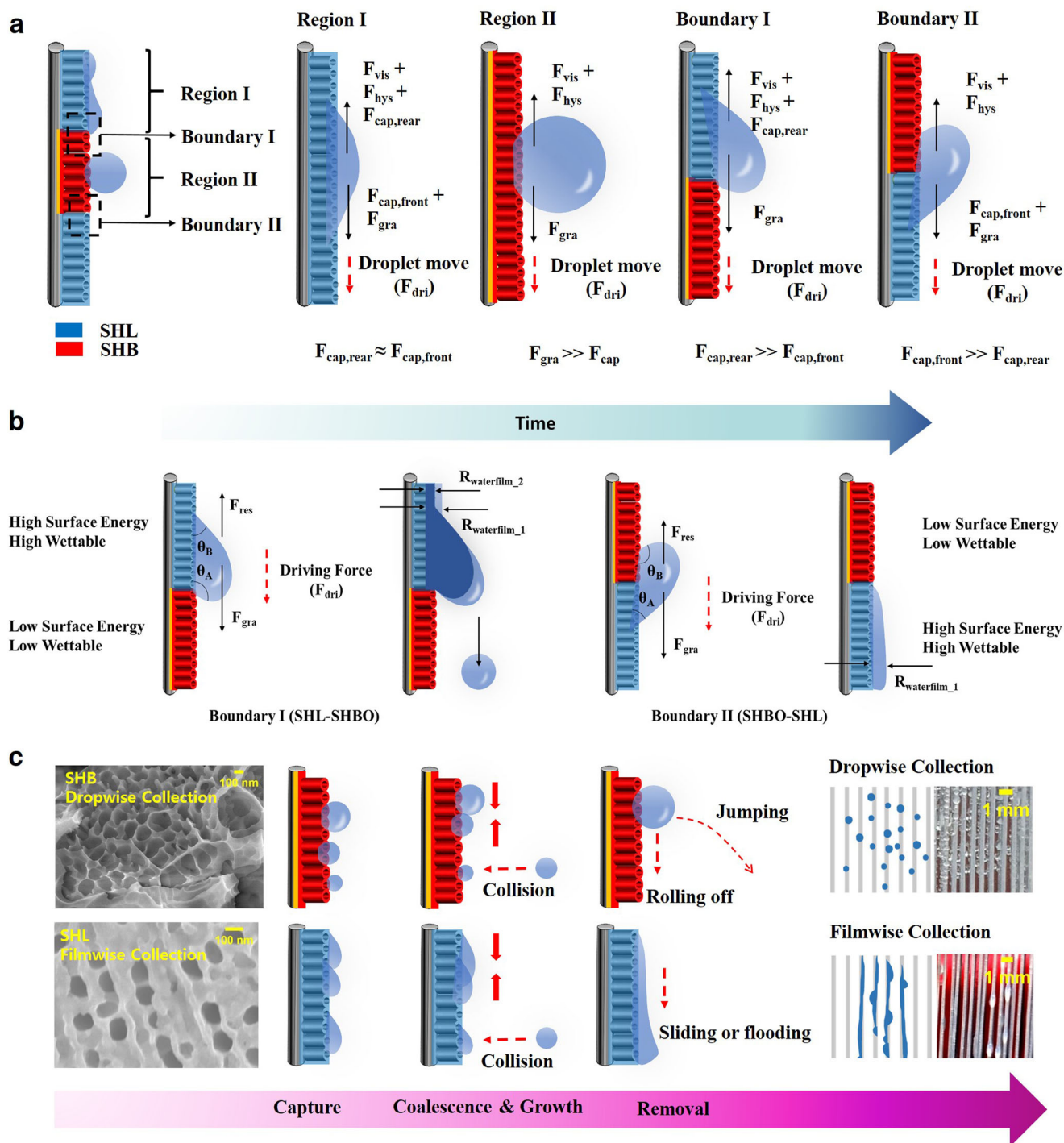
Fig. 6 | Effect of surface chemistry on water droplet collection and its mechanical simulations. a Forces acting of water droplets on the 4 types region. **b** Driving forces for two different boundary; Boundary I: from SHL to SHB surface, Boundary II: from SHB to SHL surface. **c** Harvesting mechanisms of SHB and SHL surfaces.

minimum surface. Region I represents an SHL surface, which is dominated by downward $F_{cap,front}$ and F_{gra}. The water film up to a certain thickness is key to driving the flow of water, although it is estimated that the thicker it is, the more it interferes with water deposition and mobility. Lee et al. implemented the water-adsorption mechanism of Tillandsia's trichome structure, which adorbs water from the air through the formation of a water film[41]. Region II represents the SHB or SHBO surface, and the droplets undergo dropwise collection due to a low surface energy and fall under the influence of gravity. The water droplets refresh the surface with rapid jumping movements, thereby increasing their mobility.

Boundaries I and II act to enhance the water-droplet mobility in a certain direction in the Fig. 6b. In the Boundary I from SHL to SHB, the SHB surface periodically stems the tide of the thickness growth of the liquid film accumulated along the vertical surface owing to low capture energy barriers of SHL. The growth of the liquid film increases the resistance of the film, $R_{waterfilm1}$, increasing the capture-growth energy barrier and impeding capture growth. Water droplets flowing over the water film on the SHL surface are blocked by SHBO, and when it exceeds the critical volume, it falls by gravity, and the water film is refreshed, thereby improving capture efficiency. In Boundary II, from SHB to SHL, the droplet self-propulsion is added to reinforce the flow of the droplet in a certain direction. This

wettability gradient accelerates the flow of droplets in the direction of F_{gra} on the vertical surface, thus improving their mobility[42]. Numerous extant studies have demonstrated Boundary II with the movement of self-propelled droplets[20,42,43]. This increases the drain efficiency.

Force analysis of a droplet moving on a patterned surface yields equations 7 and 8. Figure 1b shows that F_{dri} is proportional to the surface-wettability gradient. As the wettability of a solid surface is typically determined by the CA of the liquid, F_{dri} can be characterized, as follows[44,45]

$$\text{Boundary I}: \sum F_1 = F_{dri1} - F_{res} = F_{gra} - F_{vis} - F_{hys} \quad (7)$$

$$\text{Boundary II}: \sum F_2 = F_{dri2} - F_{res} = F_{gra} + F_{cap} - F_{vis} - F_{hys} \quad (8)$$

where F_{gra} and F_{cap} are gravitational ($\rho V g$: ρ and V are the density and volume of the droplet, respectively, and g is the gravity acceleration) and capillary ($2\pi R_0 \gamma (1 + \cos \theta_B)$: γ is the liquid–gas surface tension, R_0 is the droplet radius, and θ_B is the receding CAs) forces, respectively.

In the patterned samples (Supplementary Fig. 4), the area ratio (β) between the SHL and SHBO surfaces and the influences of Boundaries I and II directly affected the fog-harvesting efficiency.

Fog-harvesting mechanism

From the fundamentals of fog harvesting, it is clear that facilitating droplet capture, allowing the merging and growth of water droplets, and reducing the critical volume of water droplets leaving the surface represent the three main design concerns for enhancing performance (Fig. 6c). The wetting behavior of the heterogeneous structural surfaces significantly impacts the capture and drain process. According to previous research, the fog-harvesting techniques using hydrophobic surfaces performed better than those using hydrophilic surfaces, and this was typically due to the difference in the droplet-drain rates[44,46]. Contrarily, a hydrophilic surface exhibits a low capture barrier, which enables a few water molecules to adhere directly to the surface, increasing the surface coverage. Dissimilar to hydrophobicity, hydrophilicity encourages droplet growth, as well as the agglomeration process, which increases the fog-harvesting efficiency[14]. Although a hydrophilic, flat surface encourages droplet capture, the spreading of droplets consumes the majority of the surface area and inhibits continuous capture if it is not efficiently coalesced or eliminated.

In fog harvesting, both adsorption and absorption play important roles in the process of capturing water from fog. When fog droplets, which are tiny water droplets suspended in the air, come into contact with the SHB surface, water vapor molecules within the fog adsorb to the surface due to their attraction to the solid material. Conversely, an SHL surface is more advantageous for capturing droplets and readily forms a water film to capture conflicting droplets. In fog harvesting, absorption usually refers to the process of the collection material becoming saturated with water vapor and retaining moisture within its structure. Lee et al. applied *Tillandsia*'s *trichome structure* to a fog harvester by imitating its absorption of water droplets in the air, as well as the formation of a water film, to satisfy the necessary water demand[47]. The combination of adsorption and absorption is crucial for effective fog harvesting. Thus, the hydrophilic ratio in the wetting pattern acts as an important factor for capturing fog droplets. Supplementary Fig. 2b shows the adsorption of the fog droplets on the surface according to the surfaces with SHB and SHL ratios of 1:1, 1:2, 2:1, and 4:4.

The surface-deposited water droplets were combined with neighboring water droplets or grown by fog-flow-colliding droplets under the influence of the wetting properties of the surface. On the SHB surface (Supplementary Movie 3), tiny droplets, which were nearly circular, combined to grow into dropwise collection; conversely, on the SHL surface (mSupplementary Movie 2), they began with crescent-shaped droplet deposition and grew into filmwise collection.

When the expanding droplets reached or exceeded a specific volume, they rolled off, jumped from, slipped, or flowed down the surface (Fig. 6c).

When a droplet is suspended before falling, gravity is equal to the pinning force acting on the capillary stress[48]. Thus, it is challenging to identify the SHL surface as it forms a liquid film, whereas the SHB and SHL surfaces deviate from the surface at droplet sizes of 0.15–0.3 and 0.3–1.0 mm, respectively. The SHB-surface properties, as well as the thin-wire structure, facilitated the water-droplet movement and increased the new fog-droplet-deposition area via frequent surface renewals. In this study, the efficiency was increased by focusing on a boundary (Boundaries I and II) to maximize the capacities to harvest droplets from patterned solid samples, SHL and SHB.

Discussion

Biomimetic technology was introduced to maximize the water-droplet capture and mobility on a surface-modified solid surface, and the validity of the technology was discussed from the force analysis perspective. Further, the surface properties that could enhance the fog-harvesting efficiency by combining 3D nanostructures and patterned wettability properties with Al wires were investigated. The free-surface energy was transformed into kinetic energy when the droplets coalesced on the surface, and this caused the crucial droplets to constantly slide or detach from the surface. On the SHBO surface, as the water–oil interfacial tension was lower than the water–air one, the volume and growth rate of the water droplets increased faster and were larger than those on bare or SHB surfaces, facilitating the easy capture and growth of the droplets (Supplementary Fig. 2)[49]. The 3D nanostructured surface morphology, as well as the thickness of the nanostructured layer, affected the fog-harvesting efficiency, and the wettability patterning improved it by 120% compared with non-patterning. Among the non-patterned surfaces, the SHBO surface exhibited the best fog-harvesting performance. Regarding the surface-durability tests against corrosion and UV radiation, which are environmental pollutants, SHB and SHBO were generally resistant to both factors, and SHL was very vulnerable in the air. However, although conventional polymer samples cause secondary contamination via hardening when exposed to sunlight, the deposition surfaces of silane and Krytox oil in the atomic layer on the Al surface have been rarely observed to be cured.

The SHB surface provides a self-moved jumping for droplets of <100 μm by the over-surface energy produced from the coalescence or impact of the mist droplet with the wind[50]. To quickly harvest the small droplets captured on the surface, the SHB surface that can cause jumping must be maintained in the plate nanostructure inside the micro-wire structure. Namely, the captured droplet must maintain the Cassie–Baxter state and be prevented from transforming into the Wenzel state that pins the droplet to the surface. Particularly, the wettability gradient from hydrophobicity to hydrophilicity increases the amount of W_c as it increased the water-droplet mobility. However, to capture the fog droplets already condensed in the air by moving them to the surface using the wind, a pinning-capable Wenzel state is required. Therefore, it was divided into two coexisting (Metastable) and two partially existing (Wenzel, Cassie–Baxter, and Metastable) patterning. It was revealed that patterning imparted improved water-collection performance than the coexisting modes. SHL–SHBO–SHL provides an appropriate harmony and alignment mechanism for SHL and SHBO, which can effectively collect and transport droplets in the air on solid surfaces; β was 2, showing the hydrophilic region's significance. Improved fog efficiency is a result of boundary I increasing capture efficiency and boundary II increasing drainage efficiency. This outcome will also serve as the foundation for a sustainable, easily maintained, and environmentally friendly fog-harvesting system when it is scaled up.

Methods

Design of the nanostructured aluminum surface

The samples were prepared by winding Al wires (diameter = 0.3 mm) in a frame of 4 × 4 cm² at 0.3 mm intervals. Their shadow coefficients were 0.5 in each case. Thereafter, ultrasonic cleaning was performed in a solution mixed with ethanol and acetone for 10 min and subsequently rinsed with deionized (DI) water and air dried. To obtain a smooth and regular surface, the Al

wires were electrochemically polished for 3 min at 20 V and 15 °C in a solution containing ethanol and perchloric acid at a volume ratio of 1:4[14]. Afterward, previous Al wires were rinsed with the DI water and air dried. The polished Al wires of the anode were anodized in 0.2 M phosphoric acid at 120 V and 50 °C using a stainless steel net as the cathode. The anodized specimens were washed with ethanol and air dried.

Various wetting designs
The SHB surface was obtained by vacuum-desiccator deposition with 300 µL of trichloro(1H, 1H, 2H, 2H-perfluorooctyl)silane (Sigma-Aldrich.) at 0.08 MPa for 15 h. Thereafter, the specimens were dried in a 60 °C oven for >12 h. Next, vacuum cleaning was performed for ~30 min to remove any residual impurities on the surface. Finally, to obtain a lubricant oil (Krytox 103)-infused surface, vacuum-desiccator deposition was performed.

Conversely, the SHL surface was obtained by immersing the anodized Al wire in boiling water for 30 min; this sealing allowed for the maintenance of the hydrophilicity over time. Additionally, patterned wettable properties, i.e., the combination of SHB, SHBO, and SHL properties, were obtained using a Kapton tape (Polyimide tape) as a mask. Various conditions were tested by varying the arrangement order from the area ratios (1:1, 1:2, 2:1, and 4:4) of SHL, SHB, and SHBO. The experimental conditions and patterned wetting characteristics of the sample are displayed in Supplementary Fig. 2b.

Fog-harvesting tests
Each sample was set at RH of ≥90% and room temperature, the wind velocity was set at 3.3 ± 0.3 m/s around the center, and the amount of W_c was measured. Considering the fog dispersion of the Gaussian distribution by the turbulent air jets proposed by Cushman-Roisin, the sampled fog-test device and fog-generator-outlet interval were adjusted to 1 cm to obtain maximum fog concentration and wind speed throughout the sample[51]. Additionally, the device was designed to obtain the maximum amount of fog by making the outlet sizes of the mist and sample equal. The fog-harvesting system was implemented with a conventional fog generator and a controllable electric fan (Supplementary Fig. 1). The samples were positioned at a right angle in the direction of the fog. Using a high-resolution balance (resolution 0.01 g, OHAUS USA SPX6202KR), the devices before and after fog collection, as well as the amount of W_c, can be measured to calculate the loss of fog, sample-surface-captured droplets, and efficiency of the fog-harvesting sample.

$$\eta_w(\%) = \frac{Collected\ water(W_c)}{Generated\ fog\ water(W_g)} \times 100\% \tag{9}$$

The weight difference between the fog generator and storage before and after the experiment is indicated as *Generated fog water* (W_g) and *Collected water* (W_c), respectively. Additionally, if the mass of water remaining on the sample surface and that, which was lost water, are expressed as *Remaining water* (W_r) and *Loss Water* (W_l), respectively, the following equation can be established:

$$W_g = W_c + W_r + W_l \tag{10}$$

The water-collection efficiency is given, as follows: $\eta_w = \eta_{aero} \cdot \eta_{cap} \cdot \eta_{drain}$, where η_{ace}, η_{cap}, and η_{drain} are the aerodynamic, capture, and drain efficiencies, respectively. A previous study used the relationship between the wind's decreasing velocity as a result of the wire structure's drag to η_{aero}[52]. The amount of fog moving toward the harvester would decrease due to the conservation of mass, which causes the cross-sectional area of the wind upstream to continuously decrease with increasing drag as it passes through the construction.

$$\eta_{aero} = s \cdot \left(1 \pm \sqrt{C_0/C_d}\right)^{-1} \tag{11}$$

where C_d is the drag coefficient for an impermeable plate with an identical shape, and C_0 is the pressure drop coefficient of the harp or mesh. When considering fog harvesters with comparable overall width and height, $C_d \approx 1.18$. In relation to metal wires $C_0 = \rho_a \nu D/\mu_a \cdot (1.3S + (S/(1 - SC))^2)$, where μ_a and ρ_a stand for air's viscosity and density, respectively. For every wire, the shade coefficient $S = 0.5$, the pitch—that is, the center-to-center distance—between neighboring wires on the same row was intended to equal precisely $P = 2D$.

The capture efficiency (η_{cap}) is determined by the Stokes number (S_t), which measures how quickly suspended fog droplets react when their streamlines are disturbed by wires. Stated differently, lower values of S_t cause more droplets to flow around the wires of a harvester, whereas larger values cause more droplets to impact the wires.

$$\eta_{cap} \approx S_t \cdot \left(S_t + \frac{\pi}{2}\right)^{-1}, S_t = \frac{2\rho_w V_0}{9\mu_a} \frac{R_f{}^2}{R_w} \tag{12}$$

where ρ_w is the density of water, R_f is the fog radius, and R_w is the wire radius.

Materials characterization
The fog-harvesting behavior of the surface was observed on a camera (SM-N960N, Samsung, Korea). Field-emission SEM (Merlin Compact, Carl Zeiss, Germany) was performed at 15 kV to examine the surface morphologies of the samples. EDS (Aztec Energy X-MaxN, Oxford, U.K.) was performed to examine the mass percentages of the elements in the quantitative data of a particular region of the samples. During the analysis of the water-harvesting behavior of the samples, a humidifier (TN-H900, China) was used to produce the fog. The optical CA system (PHOENX-300 TOUCH, Surface Electro-Optics, Korea) was used to measure WCAs; the volume of the water droplet was 6 µL.

The schematics for the general and flooded conditions of the contact angle measuring processes are displayed in Supplementary Fig. 2. Instead of directly assessing the surface wettability using a sessile drop method due to the curvature of the Al wire, we assessed the contact angle on the flat Al plates, which were changed using the same technique as with the Al wires. Because the transition from the non-wetting Cassie state to the flooded Wenzel state can cause the measured contact angle to vary depending on the test conditions, we measured the contact angles under both the general condition and the flooded condition, especially for SHB surfaces under high super-saturation conditions.

Data availability
The data that support the findings of this study are available from the corresponding authors upon request.

References
1. Şen, Z. Global warming threat on water resources and environment: a review. *J. Environ. Geol.* **57**, 321–329 (2009).
2. Eliasson, J. The rising pressure of global water shortages. *Nature* **517**, 6 (2015).
3. Salehi, M. Global water shortage and potable water safety; today's concern and tomorrow's crisis. *Environ. Int* **158**, 106936 (2022).
4. Nørgaard, T. & Dacke, M. Fog-basking behaviour and water collection efficiency in namib desert darkling beetles. *Front. Zool.* **7**, 1–8 (2010).
5. Lei, J. & Guo, Z. A fog-collecting surface mimicking the Namib beetle: its water collection efficiency and influencing factors. *Nanoscale* **12**, 6921–6936 (2020).
6. Sherbrooke, W. C., Scardino, A. J., de Nys, R. & Schwarzkopf, L. Functional morphology of scale hinges used to transport water: convergent drinking adaptations in desert lizards (Moloch horridus and phrynosoma cornutum). *Zoomorphology* **126**, 89–102 (2007).

7. Comanns, P., Withers, P. C., Esser, F. J. & Baumgartner, W. Cutaneous water collection by a moisture-harvesting lizard, the thorny devil (Moloch horridus). *J. Exp. Biol.* **219**, 3473–3479 (2016).

8. Gurera, D. & Bhushan, B. Passive water harvesting by desert plants and animals: lessons from nature. *Philos. Trans. R. Soc. A* **378**, 20190444 (2020).

9. Ebner, M., Miranda, T. & Roth-Nebelsick, A. Efficient fog harvesting by stipagrostis sabulicola (Namib dune bushman grass). *J. Arid Environ.* **75**, 524–531 (2011).

10. Bai, T. et al. Cactus kirigami for efficient fog harvesting: simplifying a 3D cactus into 2D paper art. *J. Mater. Chem. A* **8**, 13452–13458 (2020).

11. Wang, X. et al. Beetle and cactus-inspired surface endows continuous and directional droplet jumping for efficient water harvesting. *J. Mater. Chem. A* **9**, 1507–1516 (2021).

12. Song, W., Zheng, Z., Alawadhi, A. H., & Yaghi, O. M. MOF water harvester produces water from Death Valley desert air in ambient sunlight. *Nat. Water* **1**, 1–9 (2023).

13. Wang, Y., Zhao, W., Han, M., Xu, J. & Tam, K. C. Tam, Biomimetic surface engineering for sustainable water harvesting systems. *Nat. Water* **1**, 587–601 (2023).

14. Dai, X. et al. Hydrophilic directional slippery rough surfaces for water harvesting. *Sci. Adv.* **4**, eaaq0919 (2018).

15. Guo, J., Huang, W., Guo, Z. & Liu, W. Design of a venation-like patterned surface with hybrid wettability for highly efficient fog Harvesting. *Nano Lett.* **22**, 3104–3111 (2022).

16. Wu, J., Zhang, L., Wang, Y. & Wang P. Efficient and anisotropic fog harvesting on a hybrid and directional surface. *Adv. Mater. Interfaces* https://doi.org/10.1002/admi.201600801 (2017)

17. Guadarrama-Cetina, J. et al. Dew collection on desert beetle skin. *Eur. Phys. J. E Soft Matter* **37**, 1–6 (2014).

18. Shi, W., Anderson, M. J., Tulkoff, J. B., Kennedy, B. S. & Boreyko, J. B. Fog harvesting with harps. *ACS Appl. Mater. Interfaces* **10**, 11979–11986 (2018).

19. Shi, W., van der Sloot, T. W., Hart, B. J., Kennedy, B. S. & Boreyko, J. B. Harps enable water harvesting under light fog conditions. *Adv. Sustain. Syst.* **4**, 2000040 (2020).

20. Yang, X., Song, J., Liu, J., Liu, X. & Jin, Z. A twice electrochemical-etching method to fabricate superhydrophobic-superhydrophilic patterns for biomimetic fog harvest. *Sci. Rep.* **7**, 1–12 (2017).

21. Feng, S. et al. Three-dimensional capillary ratchet-induced liquid directional steering. *Science* **373**, 1344–1348 (2021).

22. Cushman-Roisin, B. In *Environmental Fluid Mechanics* 141–147 (John Wiley & Sons, Inc., 2013).

23. Schemenauer, R. S. & Joe, P. I. The collection efficiency of a massive fog collector. *Atmos. Res.* **24**, 53–69 (1989).

24. Azeem, M., Noman, M. T., Wiener, J., Petru, M. & Louda, P. Structural design of efficient fog collectors: A review. *Environ. Technol. Innov.* **20**, 101169 (2020).

25. Jiang, Y., Machado, C. & Park, K. C. K. From capture to transport: A review of engineered surfaces for fog collection. *Droplet* **2**, 55 (2023).

26. Lavielle, N., Beysens, D. & Mongruel, A. Nucleation-enhanced condensation and fast shedding on self-lubricated silicone organogels. *Soft Matter* **19**, 4458–4469 (2023).

27. Fang, G., Li, W., Wang, X. & Qiao, G. Droplet motion on designed microtextured superhydrophobic surfaces with tunable wettability. *Langmuir* **24**, 11651–11660 (2008).

28. Ju, J. et al. A multi-structural and multi-functional integrated fog collection system in cactus. *Nat. Commun.* **3**, 1–6 (2012).

29. Andrews, H. G., Eccles, E. A., Schofield, W. C. E. & Badyal, J. P. S. Three-dimensional hierarchical structures for fog harvesting. *Langmuir* **27**, 3798–3802 (2011).

30. Ju, J., Zheng, Y. & Jiang, L. Bioinspired one-dimensional materials for directional liquid transport. *Acc. Chem. Res.* **47**, 2342–2352 (2014).

31. Yang, D., Od, D. G., Ramu, A. G. & Choi, D. Fabrication of enhanced corrosion protection of PEO/PFOTES nanocomposite film coatings on aluminum alloy deposited by plasma electrolytic oxidation. *Mater. Lett.* **315**, 131898 (2022).

32. Su, B., Tian, Y. & Jiang, L. Bioinspired interfaces with superwettability: from materials to chemistry. *J. Am. Chem. Soc.* **138**, 1727–1748 (2016).

33. Telmenbayar, L., Ramu, A. G., Yang, D. & Choi, D. Development of mechanically robust and anticorrosion slippery PEO coating with metal–organic framework (MOF) of magnesium alloy. *Chem. Eng. J.* **458**, 141397 (2023).

34. Söz, C. K., Yilgör, E. & Yilgör, I. Influence of the average surface roughness on the formation of superhydrophobic polymer surfaces through spin-coating with hydrophobic fumed silica. *Polymer* **62**, 118–128 (2015).

35. Yang, J. et al. New perspectives on structural parameters and hydrophobic model inspired by a superhydrophobic Cu cone-flower coating. *Mater. Des.* **206**, 109827 (2021).

36. Sheng, Q., Sun, J., Wang, Q., Wang, W. & Wang, H. S. On the onset of surface collection: formation and transition mechanisms of collection mode. *Sci. Rep.* **6**, 1–9 (2016).

37. Park, K. C., Chhatre, S. S., Srinivasan, S., Cohen, R. E. & McKinley, G. H. Optimal design of permeable fiber network structures for fog harvesting. *Langmuir* **29**, 13269–13277 (2013).

38. Lafuma, A. & Quéré, D. Superhydrophobic states. *Nat. Mater.* **2**, 457–460 (2003).

39. Nosonovsky, M. Multiscale roughness and stability of superhydrophobic biomimetic interfaces. *Langmuir* **23**, 3157–3161 (2007).

40. Quéré, D., Lafuma, A. & Bico, J. Slippy and sticky microtextured solids. *Nanotechnology* **14**, 1109 (2003).

41. Wang, B., Zhang, Y., Shi, L., Li, J. & Guo, Z. Advances in the theory of superhydrophobic surfaces. *J. Mater. Chem. A* **22**, 20112–20127 (2012).

42. Daniel, S. & Chaudhury, M. K. Rectified motion of liquid drops on gradient surfaces induced by vibration. *Langmuir* **18**, 3404–3407 (2002).

43. Liu, C. et al. Long-range spontaneous droplet self-propulsion on wettability gradient surfaces. *Sci. Rep.* **7**, 7552 (2017).

44. Yang, J. T., Yang, Z. H., Chen, C. Y. & Yao, D. J. Conversion of surface energy and manipulation of a single droplet across micropatterned surfaces. *Langmuir* **24**, 9889–9897 (2008).

45. Seo, D., Lee, J., Lee, C. & Nam, Y. The effects of surface wettability on the fog and dew moisture harvesting performance on tubular surfaces. *Sci. Rep.* **6**, 1–11 (2016).

46. Pei, W. et al. Excellent fog harvesting performance of liquid-infused nano-textured 3D frame. *Chem. Eng. J.* **409**, 128180 (2021).

47. Eral, H. B., 't Mannetje, D. J. C. M. & Oh, J. M. Contact angle hysteresis: a review of fundamentals and applications. *Colloid Polym. Sci.* **291**, 247–260 (2013).

48. Choo, S., Choi, H. J. & Lee, H. Water-collecting behavior of nanostructured surfaces with special wettability. *Appl. Surf. Sci.* **324**, 563–568 (2015).

49. Nørgaard, T., Ebner, M. & Dacke, M. Animal or plant: which is the better fog water collector? *PLoS One* **7**, e34603 (2012).

50. Boreyko, J. B. & Chen, C. H. Self-propelled dropwise condensate on superhydrophobic surfaces. *Phys. Rev. Lett.* **103**, 184501 (2009).

51. Nioras, D., Ellinas, K., Constantoudis, V. & Gogolides, E. How different are fog collection and dew water harvesting on surfaces with different wetting behaviors? *ACS Appl. Mater. Interfaces* **13**, 48322–48332 (2021).

52. de Dios Rivera, J. Aerodynamic collection efficiency of fog water collectors. *Atmos. Res.* **102**, 335–342 (2011).

Author contributions
Daejeong Yang: Conceptualization, Investigation, Writing – original draft, Revision Visualization. A.G. Ramu: Investigation, Data curation, Visualization, Revision. Dongjin Choi: Conceptualization, Supervision, Writing – original draft, Revision, Supervision, Project administration, Funding acquisition.

Competing interests
The authors declare no competing interests.

Additional information
Supplementary information The online version contains supplementary material available at
https://doi.org/10.1038/s41545-024-00317-6.

Correspondence and requests for materials should be addressed to Dongjin Choi.

Reprints and permissions information is available at
http://www.nature.com/reprints

Publisher's note Springer Nature remains neutral with regard to jurisdictional claims in published maps and institutional affiliations.